Revista Internacional de Investigación e Innovación Tecnológica

Página principal: www.riiit.com.mx

Polymeric coating reinforced with Co_2O_3 nanoparticles (1 wt%) for improved mechanical, thermal, and corrosion resistance on AISI 1018 carbon steel

Recubrimiento polimérico reforzado con nanopartículas de Co_2O_3 (1% en peso) para mejorar la resistencia mecánica, térmica y a la corrosión en acero al carbono AISI 1018

González-Vázquez, J.A.[AB]*, Flores-Villaseñor, S.E.[C], Ríos-Hurtado, J.C.[C], García-Rentería, M.A.[C]

[A] Centro de Estudios e Investigaciones Interdisciplinarias, Universidad Autónoma de Coahuila, Ciudad Universitaria. Carretera México km 13, Arteaga, Coahuila (*https://orcid.org/0000-0001-8681-9022)
[B] Universidad Tecnológica de la Región Centro de Coahuila, Carretera 57 Norte km 14.5 Monclova-Sabinas, Monclova, Coahuila, México (*https://orcid.org/0000-0001-8681-9022).
[C] Facultad de Metalurgia, Universidad Autónoma de Coahuila, Carretera 57Km 4.5, Zona Universitaria, Monclova, Coahuila, México (https://orcid.org/0000-0002-0654-0046, https://orcid.org/0000-0002-2346-4540, https://orcid.org/0000-0002-0654-0046).
jose.antonio.gonzalez@utrcc.edu.mx*; sergio.villasenor@uadec.edu.mx; jorgerios@uadec.edu.mx; marcogarciarenteria@uadec.edu.mx

Technological innovation: Modification of thermal and mechanical properties under tensile stress and improved corrosion resistance in saline environments.

Industrial application area: Engineering of anticorrosive coatings.

Received: March 05th, 2025
Accepted: September 22th, 2025

Resumen

Este estudio analizó la mejora de las propiedades mecánicas, térmicas y anticorrosivas de recubrimientos de poliuretano (PU) mediante la incorporación de nanopartículas de óxido de cobalto (Co_2O_3) al 1% en peso. A diferencia de los aditivos convencionales, que funcionan por pasivación o sacrificio, el Co_2O_3 se evaluó como un refuerzo multifuncional. La síntesis se llevó a cabo mediante mezcla de polioles y antiespumantes a 25 °C, incorporando las nanopartículas a la matriz polimérica. Las muestras se caracterizaron por FTIR, DRX, TGA, ensayos de tracción (ASTM D638) y pruebas electroquímicas en NaCl al 5%. El FTIR confirmó las bandas del PU y una señal a 570 cm^{-1} asociada al Co_2O_3, mientras que el DRX evidenció planos cristalográficos (311), (111) y (440). El TGA mostró mayor estabilidad térmica en el sistema reforzado, con pérdida de masa del 82% a 456.39 °C frente al 90% a 440.15 °C en el PU puro. En tracción, el recubrimiento con Co_2O_3 alcanzó 16.55 MPa respecto a 9.58 MPa del PU. No obstante, el análisis electroquímico

reveló un aumento en la velocidad de corrosión (0.047 mpy vs. 0.008 mpy), atribuible a aglomeración y defectos. En conclusión, el Co_2O_3 mejoró el desempeño térmico y mecánico, pero requiere optimizar su dispersión para garantizar la protección anticorrosiva.

***Palabras clave*:** Corrosión, Recubrimiento, Nanopartículas, Polimérico, Potenciodinámico.

Abstract

This study analyzed the improvement of the mechanical, thermal, and anticorrosive properties of polyurethane (PU) coatings by incorporating cobalt oxide (Co_2O_3) nanoparticles at 1 wt%. Unlike conventional additives, which act mainly through passivation or sacrificial mechanisms, Co_2O_3 was evaluated as a multifunctional reinforcement. The synthesis was carried out by mixing polyols and antifoaming agents at 25 °C, incorporating the nanoparticles into the polymeric matrix. The samples were characterized by FTIR, XRD, TGA, tensile tests (ASTM D638), and electrochemical measurements in 5% NaCl solution. FTIR confirmed the PU bands and a signal at 570 cm^{-1} associated with Co_2O_3, while XRD revealed crystallographic planes (311), (111), and (440). TGA showed higher thermal stability in the reinforced system, with 82% mass loss at 456.39 °C compared to 90% at 440.15 °C in pure PU. In tensile tests, the Co_2O_3-reinforced coating reached 16.55 MPa compared to 9.58 MPa for PU. However, electrochemical analysis revealed an increased corrosion rate (0.047 mpy vs. 0.008 mpy), attributed to nanoparticle agglomeration and defect formation. In conclusion, Co_2O_3 enhanced the thermal and mechanical performance but requires optimized dispersion to ensure anticorrosive protection.

***Keywords*:** Corrosion, Coating, Nanoparticles, Polymeric, Potentiodynamic.

1. Introduction

Metallic materials whose main component is iron (Fe), known as ferrous materials, as well as certain non-ferrous alloys, are routinely attacked by the surrounding environment, generating corrosion defects in the form of pits that compromise the structural function of the material (Wang, 2025). This phenomenon contributes to an increase in the vibration period and a reduction in the service life of steel components (Disarno, 2021). The chemical and electrochemical reactions occurring on the substrate surface gradually degrade the physical properties of the material, such as oscillation resistance, and generate stress concentrators, as reported by Kotni (2023) and Balangao (2024). The degradation of the material not only represents functional damage in engineering but also involves significant economic losses, estimated between 3% and 4% of the gross domestic product (GDP) in industrialized developing countries (Iannuzzi, 2022).

Ferrous materials are classified, according to their carbon content, into three groups: low carbon (<0.25% C), medium carbon (0.25–0.70% C), and high carbon (0.70–1.05% C), all of which are used in the manufacturing of equipment and structures (Antonio, 2020). If these components lose their mechanical properties, there is a potential risk of structural failure, especially in critical elements such as pipes or stationary pressure cylinders. One of the most widely used steels in the industry is ASTM A36 or AISI 1018, due to its adequate mechanical properties and low cost; however, it is highly susceptible to

corrosion processes, resulting in surface degradation, mass loss, and alteration of its mechanical functions (Márquez, 2022).

The chemical and electrochemical phenomena that induce corrosion cannot be completely stopped (Gómez, 2020). Nevertheless, several public and private research groups have developed strategies to reduce the rate of degradation, focusing on the formation and application of different types of protective coatings, including polymeric, metallic, and ceramic coatings. In this context, polyurethane (PU) has been widely employed in industrial coatings due to its high elasticity, good adhesion, wear resistance, and relative chemical stability. However, the efficiency of PU as an anticorrosive barrier is limited by the presence of pores and microdefects that allow the permeation of aggressive species.

The present research article analyzes recent trends in the development of polymer composite coatings, known as hybrid films, reinforced with metal oxide nanoparticles (NPs). These coatings have demonstrated a significant reduction in corrosion rate compared to systems without nanoparticle reinforcement (Elfadel et al., 2023). Among these systems, cobalt (III) oxide nanoparticles (Co_3O_4) stand out due to their physicochemical properties. Recent studies report that Co_3O_4 NPs exhibit average sizes in the nanometric range (≈13 nm), a high specific surface area (~92 m^2/g), and a spinel structure, which favors their ability to fill microdefects in the polymeric matrix and reinforce its internal network. In contrast, other oxides such as CoO, MnO_2, or NiO show lower structural stability and less effectiveness in forming anticorrosive barriers. Thus, Co_3O_4 not only acts as an inorganic pigment but also as a multifunctional reinforcement that enhances the mechanical strength, thermal stability, and anticorrosive performance of the system (Deyab, 2024).

Currently, different types of physical anticorrosive barriers are commercially available, such as polymeric (epoxy resins), metallic (galvanized coatings), and refractory systems. However, these coatings involve high costs and complex application processes (Nartita, 2021). Since hybrid coatings with nanoparticles demonstrate superior properties, the hypothesis is proposed that the incorporation of Co_2O_3 into a PU matrix will improve its tensile strength, thermal stability, and anticorrosive protection of AISI 1018 carbon steel compared to polyurethane alone (PU). For this reason, the main objective of this research is to develop polyurethane-based coatings with enhanced thermal, mechanical, and anticorrosive properties, specifically designed for application in high-salinity environments, such as those observed in coastal or industrial areas.

2. Methodology

The experimental methodology of this research was divided into nine main stages. First, the polyurethane (PU) resin was synthesized from commercial reagents, and cobalt oxide (Co_2O_3) nanoparticles were obtained through a precipitation and calcination process. The nanoparticles were then structurally characterized using X-ray diffraction, while the hybrid PU + Co_2O_3 system was formulated by incorporating 1 wt% of NPs into the polymeric matrix to develop an anticorrosive coating.

Subsequently, chemical and thermal analyses (FTIR and TGA) were performed to identify functional groups and evaluate the thermal stability of the coatings. The mechanical properties of both PU and the hybrid system were then assessed through tensile tests, following the ASTM D638 standard.

AISI 1018 steel substrates were mechanically prepared by abrasive cleaning to ensure proper adhesion, and the coatings were applied using the dip-coating technique, employing both pure PU and PU reinforced with nanoparticles. Finally, electrochemical tests were conducted in a 5% saline medium to determine the anticorrosive performance of the developed systems.

Overall, this methodology enabled the synthesis, characterization, and evaluation of hybrid polyurethane coatings reinforced with cobalt oxide nanoparticles, comparing their thermal, mechanical, and anticorrosive properties with those of conventional PU.

2.1. Polyurethane (PU) resin synthesis

The polyurethane (PU) resin was synthesized using commercially available reagents under controlled conditions at room temperature (25–30 °C). The process consisted of mechanically mixing the components at 1000 rpm and a pH between 6.5 and 9. The addition of the hardener initiated the polymerization reaction, forming long macromolecular chains, while the defoaming agent prevented the expansion of the resin volume, avoiding PU foam formation, which is unnecessary for anticorrosive coatings. Once mixed, the curing process began at room temperature. Polyurethane resins can also incorporate pigments and additives to modify color and functional properties. For the formulation used in this research, Part A included an anionic polyacrylate Bayhydrol XP 2546 (48%), mineral oils Drewplus T-4201 (1% antifoaming agent), Hydropalat 140 (1% surfactant), Ultralube-816 (1% wax powder), hydrated magnesium silicate MK Deuteron (1% matting agent), deionized water, and DSX 514 (rheological additive at 3.5%). Part B consisted of Bayhydur XP 2547, a hexamethylene diisocyanate (HDI) hardener at 20%. The reagents were grouped into two components (Part A and Part B), as shown in Table 1.

Table 1. Formulation to produce PU resin, 25-30 °C, pH 6.5-9.

Parts	Tradename	Product	Function	Ratio %	pH
Part A	Bayhydrol XP 2546	Anionic polyacrylate	Polyol	48	7-9
	Drewplus T-4201	Siliceous mineral oil	Antifoaming agent	1	-
	Hydropalat 140	Surfactant	Surfactant additive	1	6.5-7.5
	Deionized water	-	-	26.50	7
	DSX 1514 (8% de H_2O)	Polyurethane rheological additive	Rheological modifier	3.50	6.5-7.5
Part B	Bayhydur XP 2547	HD (hexamethylene diisocyanate)	Hardener	20	7.9-8.6
		Total		100	

The procedure for the preparation of the polyurethane (PU) resin consisted of carrying out the mixture according to the percentages of the components mixed at room temperature. In preparation of 5 liters (L) of coating, 2.4 L of anionic polyacrylate, 0.05 L of antifoaming agent, 0.05 L of surfactant additive, 1.32 L of deionized water, and 0.175 L of rheology modifier were used for Part A. For the remaining 20% of Part B, 1 L of hexamethylene diisocyanate was used. The resin curing process began immediately after mixing parts A and B. The volume relationship is provided in Table 2.

Table 2. Quantities to produce 5 L of resin.

Components	Quantity (L)
Part A	4
Part B	1

The polymerization of polyurethane results from the reaction between a diisocyanate and a polyol (Figure 1), producing urethane bonds (–O–CO–NH–) (Das, 2020). The isocyanate (–NCO) groups of the diisocyanate react with the hydroxyl (–OH) groups of the polyol, generating a polymeric structure with repetitive urethane linkages. Catalysts and additives regulate the reaction rate and final polymer architecture. The type and proportion of polyol determine the flexibility of the material, while the choice of diisocyanate influences rigidity and thermal stability (Souza, 2021). Depending on the formulation, polyurethanes can be flexible, semi-rigid, or rigid, enabling applications across different industrial sectors.

Secondary reactions may occur, such as urea bond formation (–NH–CO–NH–) when isocyanates react with water, releasing CO_2. This process is fundamental in producing polyurethane foams, where the gas acts as an expanding agent, creating cellular structures that reduce density and improve thermal insulation (Wu, 2024). The final structure depends on the ratio of isocyanate to hydroxyl groups, as well as the use of additives like surfactants, rheological modifiers, and antifoaming agents, which improve stability, control bubble formation, and optimize processability (Rodriguez, 2020).

To confirm functional groups, FTIR analysis was performed in the 4000–500 cm^{-1} range, with a resolution of 4 cm^{-1} and 32 scans per sample.

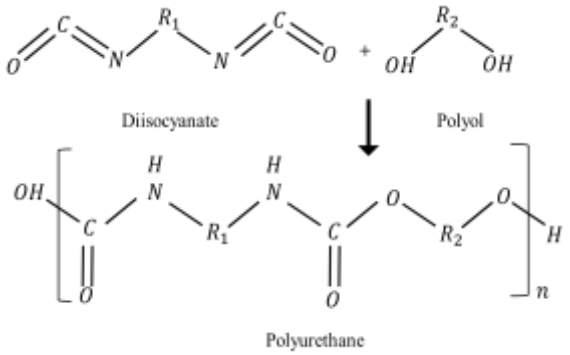


Figure 1. Polymerization reaction of diisocyanate and polyol (Panda, 2018).

2.2. Synthesis of Co_2O_3 nanoparticles (NPs)

For the preparation of Co_2O_3 NPs, the precursor salts technique was used, the reagents utilized are shown in Table 3.

Table 3. Reagents for synthesis of Co_2O_3 NPs.

Reagents	Trade name	Molar mass (g/mol)	Concentration (%)	Quantity SI
Sodium dodecyl sulfate (SDS)	Carl Roth	288.4	97	0.139 g
Distilled water	-	-	-	300 mL
Sodium carbonate (Na_2CO_3)	Carl Roth	106	99.5	1.59 g
Cobalt chloride ($CoCl_2$)	Carl Roth	237.9	99	1.19 g

For the synthesis of Co_2O_3 NPs, the surfactant solution was made by mixing 0.139 g of sodium dodecyl sulfate (SDS) in 100 mL of deionized water at room temperature. The precipitating solution was 1.59 g of sodium carbonate (Na_2CO_3), in 100 mL of water. Subsequently, the solution of precursor salts was prepared by adding 1.19 g of cobalt chloride ($CoCl_2$) to 100 mL of water. The three solutions were incorporated at an ambient temperature of 25 °C for a period of 6 h, until the solution turned to a violet color,

which was followed by a drying process at 80 °C for 2 h, and finally a heat treatment at 1000 °C for 5 h. The chemical reaction is shown below (Eq 1).

$$3CoCl_2 + 3Na_2CO_3 + 3H_2O + O_2 \rightarrow Co_3O_4 + 6NaCl + 3CO_2 \uparrow + 3H_2O \quad \textbf{(Eq. 1)}$$

After the calcination process, the Co_2O_3 NPs nanoparticles were prepared for the XRD analysis technique to determine the crystallographic phase, and planes present in the microstructure of metal oxides.

2.3. X-ray diffraction analysis (XRD), Co_2O_3 NPs

The microstructural analysis of the cobalt (III) oxide (Co_2O_3) nanoparticles was performed using the X-ray diffraction (XRD) technique in powder, with the aim of identifying the existing crystalline phase, evaluating the level of crystallinity, and estimating the average size of the crystallites. For this purpose, an X-ray diffractometer configured in the Bragg-Brentano geometry (θ-2θ) was used, equipped with a copper radiation source (Cu Kα) with a wavelength of 1.5406 Å. The operating conditions of the equipment were determined under a voltage of 40 kV and a current of 30 mA. The scan was carried out continuously, encompassing an angular range of 2θ from 10° to 80°, with a scan rate of 2° per minute and a pitch size of 0.02°, using a counting time of 1 second per feed. In the sample preparation process, the dry nanoparticles were finely pulverized and deposited on a low-fluorescence glass sample holder, ensuring a smooth and homogeneous surface to prevent preferential orientation effects during the measurement procedure. Using the Scherrer equation, the average size of the crystallites that make up the NPs was estimated from the widening of the diffraction peaks (Fatimah, 2023). It is based on the principle that the diffraction peaks of crystalline materials widen as the size of the crystallite decreases because of structural confinement (Bokuniaeva, 2019). The equation is expressed.

$$D = \frac{K\lambda}{\beta cos\theta} \quad \textbf{(Eq. 2)}$$

Where:
D is the average size of the crystallite in nanometers, K is a shape constant with values between 0.89 and 0.94 (typically 0.9 for approximately spherical particles), λ represents the wavelength of the X-ray radiation used (for Cu Kα, λ=0.15406 nm), β is the total width at half-height (FWHM) of the diffraction peak in radians, and θ is the diffraction angle corresponding to the peak of interest (Chérif, 2023). In the practical application of this equation, the XRD pattern of the material is first obtained, and the characteristic peaks of the crystalline phase are identified. Subsequently, a high-intensity peak is selected and its width at half height (FWHM) is measured, preferably correcting for instrumental widening. Then, the angle θ of the peak is determined and the values in the Scherrer equation are substituted to obtain the average size of the crystallite.

Despite its usefulness, the Scherrer equation has certain limitations. It does not distinguish between crystallite size and particle size, as a particle can be composed of multiple crystallites (Basak, 2022). For the DLS analysis, a dilute suspension of the calcined nanoparticles was prepared in ultrapure water. Approximately 1 mg of sample was dispersed in 10 mL of water and ultrasonicated for 15 minutes to ensure homogeneous dispersion and minimize crowding. The measurement was made using a particle size analyzer by DLS (e.g., Zetasizer Nano ZS, Malvern Instruments), employing a quartz cuvette with low optical dispersion and maintaining a constant

temperature of 25 °C during the measurement. The equipment was configured with a detection angle of 173° (backscatter), and multiple runs per sample (usually three measurements per run, with five runs per sample) were used to ensure repeatability and accuracy of the results.

2.4. Preparation of anticorrosive coating (hybrid film)

Figure 2 below shows the formulation process of an anticorrosive coating based on polyurethane modified with 1 wt% cobalt oxide (Co_2O_3) nanoparticles. In the first stage, the Co_2O_3 nanoparticles are incorporated into an anionic polyacrylate dispersing medium, called Part A, represented in a beaker. This initial mixture is subjected to mechanical agitation to achieve a homogeneous distribution of the nanoparticles. This mixture is then transferred to a second beaker, where it is subjected to mechanical agitation for 8 to 10 minutes at a speed of 1000 rpm, keeping the temperature controlled at 25 °C. This process ensures adequate dispersion of the nanoparticles within the polymer matrix. Part B (hardener or curing agent) is then incorporated into the system in agitation, as indicated by the downward curved arrow. This addition initiates the chemical cross-linking process between the functional groups of polyol (Part A) and isocyanate (Part B), resulting in the formation of a continuous polymer network, thus constituting the final anticorrosive coating (Izarra et al., 2021).

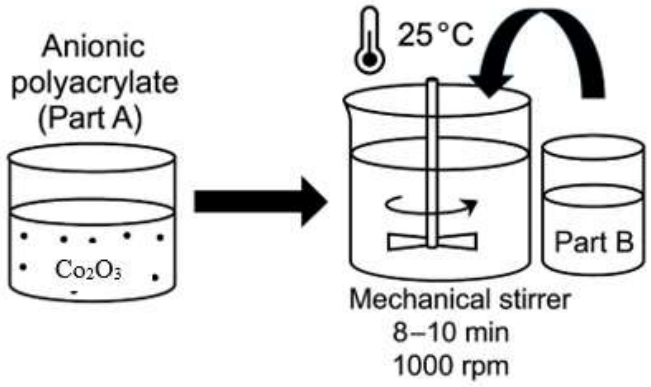


Figure 2. Preparation for hybrid coating.

2.5. TGA Analysis PU + 1 wt% Co_2O_3

To evaluate the thermal stability of the polyurethane (PU) coating modified with 1 wt% cobalt (III) oxide (Co_2O_3) nanoparticles by weight, a thermogravimetric analysis (TGA) was carried out. This technique allows the mass loss of the material to be recorded as a function of temperature, thus identifying the thermal events associated with the decomposition of the polymeric system. The analysis was carried out in an inert nitrogen atmosphere to avoid oxidation processes during heating. The sample was subjected to a constant heating rate of 10 °C per minute, starting from an initial temperature of 25 °C and reaching a maximum temperature of 800 °C. This thermal range is suitable for identifying the different stages of thermal degradation of polyurethane, as well as the influence that the incorporation of metal nanoparticles has on the thermal resistance of the system. The test made it possible to determine the thermal degradation events characteristic of the polymer, such as the rupture of urethane bonds and the decomposition of the organic matrix, as well

as the percentage of residual mass at the end of the analysis.

2.6. Mechanical properties

Silicone molds were made, with dimensions where the width of the narrow section (W) is 13 mm ± 0.5 mm, the overall length (Lo) is 165 mm, the distance between jaws (D) is from 115 mm ± 5 mm, the length of the narrow section (L) is from 57 mm ± 0.5 mm, the length of the caliber (G) is from 50 mm ± 0.25 mm, there is an overall width (Wo) of 19 mm, the fillet radius (R) is 76 mm ± 1 mm, and the thickness (T) is 3.2 mm ± 0.4 mm, in accordance with the specifications of ASTM D638 (2022) (as shown in Figure 3). The two composite systems were formulated in accordance with the procedure referred to in section 2.4. The specimens were subjected to a curing process for a period of 24 h at a temperature of 30 °C and then stored for at least 48 h under normal laboratory conditions (23 °C) and with a relative humidity of 50%. The analysis of the mechanical behavior of materials is essential in various industrial and scientific applications. One of the main tools to evaluate the strength and stiffness of a material is the study of the stress-strain curve, which provides key information about its elastic and plastic properties. This relationship is described by parameters such as modulus of elasticity, yield strength, tensile strength, and maximum strain before fracture (Rizzante, 2019).

The modulus of elasticity (E), also known as Young's modulus, represents the ability of a material to resist elastic deformation when a load is applied to it (Raju, 2018). It is defined as the slope of the elastic region of the stress-strain curve and is expressed as:

$$E = \frac{\sigma}{\varepsilon} \qquad \textbf{(Eq. 3)}$$

Where: *E* is the modulus of elasticity (MPa or GPa), σ is the applied stress (MPa) and ε is the unit strain (dimensionless).

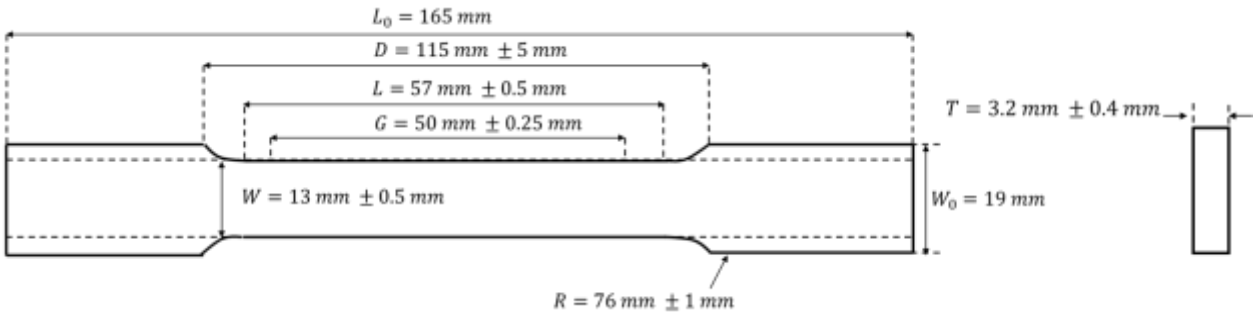


Figure 3. Specimen dimension model ASTM D638 (2022).

2.7. Cutting of steel substrates

Below is the simplified design of the substrates used for the application of the anticorrosive coating. A medium carbon AISI 1018 steel was chosen as the main material due to its commercial availability, excellent mechanical properties, and compatibility with protective coatings. The samples were cut from a steel plate using a band saw cooled with soluble oil, to prevent overheating and possible microstructural modifications in the material. Each substrate was fabricated with dimensions of 30 mm × 30 mm × 1.25 mm, as evidenced in Figure 4. In total, three samples were used, which were subsequently subjected to cleaning and surface preparation procedures to ensure optimal coating adhesion.

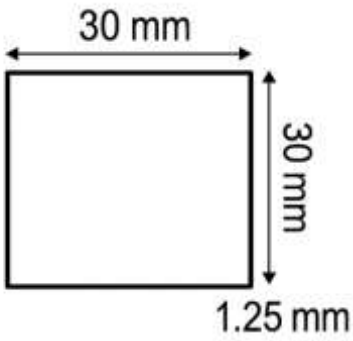


Figure 4. Dimensional design of the substrates.

Before the application of an anticorrosive coating, surface preparation of the steel is of utmost importance. The adequate anchoring profile must be guaranteed to ensure that the adhesion of the coating is carried out correctly (Vandame, 2020) and will not result in spaces or corrosion blistering which would allow for the reduction of oxygen and the promotion of areas with acidic pH; thus, anodic zones (Kim et al., 2021) & (Bogatu et al., 2023). The samples were subjected to an abrasive grinding process (blasting) with an angle shot from the W Abrasive brand with an anchor profile range of 1.5 to 2.3 mils.

2.8. Coating application on substrate

The application process of coating systems is shown in Figure 5. Two beakers were used in which the prepared systems were deposited. Two coatings were formulated: the first consisted of polyurethane (PU) and the second of PU reinforced with 1 wt% nanoparticles (NPs), following the established methodology. Each system was placed in separate beakers, and the steel substrates were immersed at a controlled speed of 0.6 cm/s, held in the solution for 30 seconds to ensure proper adhesion of the coating, and then withdrawn at a speed of 0.5 cm/s. Controlling both the immersion and withdrawal speeds is crucial, since these parameters directly influence the thickness and uniformity of the deposited film on the steel substrate.

Subsequently, the specimens were kept under curing conditions at room temperature (30 °C) for 24 hours. This method, known as dip-coating, is simple to perform and incurs no additional cost, as it does not require the acquisition of special equipment. It should be noted that only the front face of both samples was submerged, since during electrochemical analysis it is necessary for the circuit to be closed through the back of the substrate.

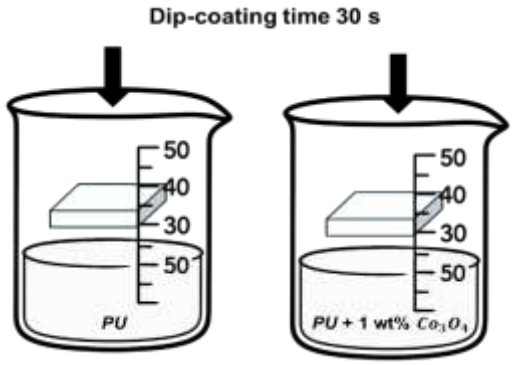


Figure 5. Dip-coating process.

2.9. Electrochemical analysis

When electron transfer occurs during the Open Circuit Potential (OCP) electrochemical process, it has been shown that no external electrical energy is applied to the cell to increase reaction kinetics and determine the anodic and cathodic behavior, which results in potentiodynamics polarization curves. Critical values, such as the Ecorr (corrosion potential) are generated, allowing us to identify whether the system exhibits noble or active behavior when the corrosion potential is near 0 mV. Using the Tafel extrapolation technique, we can determine the logarithm of the current density icor (A/cm^2), thus resulting in the corrosion rate of the system as illustrated in Figure 6. The i_{cor} quantity is defined as, (G102-89, 2023):

$$i\,cor = \frac{I\,cor}{A} \qquad \textbf{(Eq. 4)}$$

Where "i cor" is the corrosion current density, "I cor" the current intensity and "A" area
The equivalent weight (EW) is given by equation 5:

$$EW = \frac{W}{n} \qquad (\boldsymbol{Eq.5})$$

Where "W" is the element atomic weight, and "n" number of electrons transferred in the oxidation reaction.

The corrosion rate (CR) of the system in terms of the penetration rate is defined as:

$$CR = K_1 \frac{i\ cor}{\rho} EW \qquad (\boldsymbol{Eq.6})$$

Where "K1" is the constant value "3.27x10-3 mm.g/μA.cm.year", and "ρ" density of element.

A corrosion rate analysis was conducted using an Interface 1010E potentiostat, model type B 720-00160, along with a ParaCell™ Electrochemical Cell Kit. In this cell, a 5% saline solution was introduced, in accordance with the ASTM B117 (2019) standard. The contact area was 3 cm², evaluated at three points (spots) of each of the samples corresponding to the two coating systems.

For the electrochemical measurement, three electrodes were used: a silver chloride reference electrode (Ag/AgCl), a graphite electrode as the counter electrode, and as the working electrode, coated 1018 steel samples were used, functioning as sacrificial electrodes. The obtained data were processed using the Echem Analyst software, with the purpose of determining the corrosion potential (OCP) and corrosion current density values. The measurement parameters used were as follows: exposure time of 15 minutes, scan rate of 1.66 mV/s, material density of 7.87 g/cm³, and an open circuit potential (OCP) recorded at -514 mV.

3. Results and discussion

3.1. NPs Co_2O_3 XRD

According to the results of X-ray diffraction shown in Figure 6, it was determined that the Miller indices for the crystallographic planes were 440 for 2θ at 65°, 511 at 59°, 422 at 56°, and 400 at 44° (Ferreira, 2023). The highest peaks were at 38° (311), 33° (220), and 20.5° (111) (Bali, 2024). The intensity of these peaks correlates with the cobalt oxide (Co_2O_3) planes as indicated in the pattern graph. The diffraction peaks correspond to the cubic spinel phase of cobalt oxide (Co_2O_3), indicating that the sample has no other secondary phases or impurities (Rabee, 2022).

The position of the peaks coincides with the data reported in the diffraction database (ICDD PDF 42-1467), confirming the expected crystal structure. The average size of the crystallite (D) can be calculated using Scherrer's equation:

$$D = \frac{(0.9)\lambda}{\beta cos\theta}$$

The average size of the Co_2O_3 crystallite, calculated using the Scherrer equation at the most intense peak (311), is approximately 16.83 nm. This value indicates that the sample is composed of nanoparticles with high crystallinity, which can influence its optical, catalytic, and electrochemical properties (Daranfed, 2020).

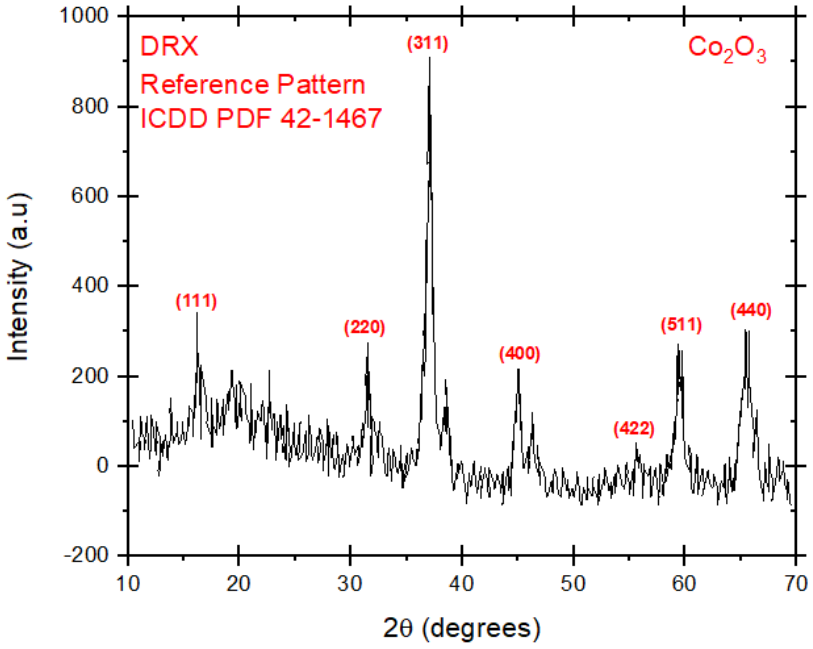


Figure 6. X-ray diffraction pattern for the Co_2O_3 NPs.

The dynamic light scattering (DLS) analysis conducted on cobalt oxide (Co_2O_3) nanoparticles offers comprehensive insights into their size distribution within an aqueous medium. The findings indicate that most of the NPs fall within the 50 to 100 nm range at 25 °C, with the highest intensity peak observed at around 75 nm ± 165 nm. This distribution pattern suggests that the sample primarily consists of well-dispersed particles in the solution (Tharasan, 2022). However, a minor fraction of larger particles, ranging from 200 to 350 nm, is also detected, pointing to the potential formation of aggregates (Valappil, 2019). The Gaussian fitting curve reveals an asymmetric distribution, with a pronounced presence in the nanometric region.

When comparing these results with the crystallite size estimated through X-ray diffraction (XRD) and the Scherrer equation, which yielded an average size of 16.83 nm, it becomes evident that the nanoparticles detected via DLS are composed of multiple crystallites clustered together (Freitas, 2019). This variation is typical in materials synthesized using colloidal or controlled precipitation methods, where individual crystallites tend to aggregate, forming larger particles (Vennela, 2019). Furthermore, the size determined by DLS corresponds to the hydrodynamic diameter of the suspended particles, encompassing the surrounding solvent layer and potential electrostatic interactions, which affect the measured values (Saied, 2021). As shown in Figure 7. The chemical synthesis of nanoparticles is a commonly employed method for generating nanomaterials with tailored properties. However, a significant challenge associated with this approach is the variability in nanoparticle size, which can greatly influence their characteristics and potential applications. This inconsistency arises from various factors during the synthesis process, including precursor concentration, reaction temperature, reaction duration, and stirring speed. These parameters are crucial in determining nucleation and growth rates, and any uncontrolled fluctuations can lead to a broad and non-uniform size distribution

(Huang, 2023). For instance, changes in temperature can modify the nucleation and growth dynamics, producing nanoparticles of varying dimensions (Kumari, 2023).

The drawbacks of nanoparticle size variability are numerous. A broad size distribution can compromise the uniformity and reproducibility of material properties, which is essential for applications requiring consistent performance. Additionally, nanoparticles of different sizes may exhibit variations in reactivity and stability, affecting their effectiveness in various materials engineering fields (Vera, 2018). Another critical issue is the tendency of nanoparticles to aggregate, particularly when size disparities exist. Agglomeration can significantly impact the surface properties and functionality of nanoparticles, diminishing their efficiency in applications such as catalysis or anticorrosive coatings. In the latter case, aggregation can lead to the formation of structural gaps, facilitating the penetration of corrosive ions and thereby compromising the protective capabilities of the coating (Valério, 2022).

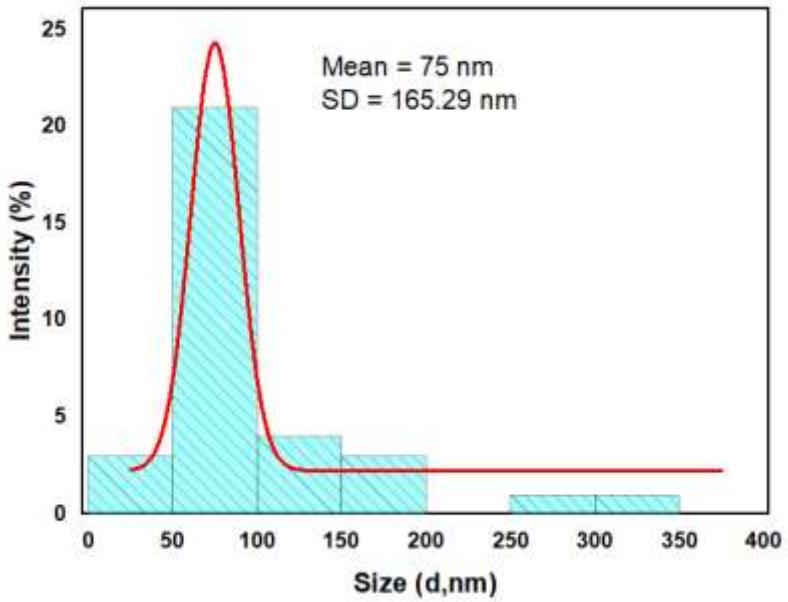


Figure 7. Size distribution Co_2O_3 NPs

3.2. FTIR and TGA of polyurethane (PU + 1wt% Co_2O_3)

The Fourier Transform infrared spectroscopy analysis revealed the vibration and energy band characteristics of the functional groups present in the polyurethane bonds. The results from this characterization analysis, as illustrated in Figure 8. Polyurethane (PU) is a polymer synthesized through the reaction between diisocyanates and polyols, resulting in the formation of urethane bonds (-NH-COO-) (Troya, 2024). In the FTIR spectrum, several characteristic bands of PU can be identified; 3552 cm^{-1} (O-H) and 3303 cm^{-1} (N-H): These bands correspond to the stretching vibrations of hydroxyl (O-H) and amine (N-H) groups, which originate from the functional groups of polyurethane. Their presence indicates the existence of hydrogen bonding within the PU structure (Ren, 2022). 2926 cm^{-1} (C-H): This band is associated with the stretching vibrations of C-H bonds present in the hydrocarbon segments of the polyurethane backbone (Głowińska, 2024). 1661 cm^{-1} and 1579 cm^{-1} (C=O and N-H):

These bands correspond to the stretching vibration of the carbonyl group (C=O) in the urethane bond and the bending vibration of the N-H bond, respectively (Li, 2023). The position of these bands may shift due to intermolecular interactions with nanoparticles (Kausar, 2021). 1082 cm^{-1} and 1020 cm^{-1} (C-O-C): These bands correspond to the stretching vibrations of the ether (C-O-C) groups in the polyurethane structure (Khuyen, 2021).

A shift in these bands may indicate interactions between the nanoparticles and the polymeric matrix (Lysenkov, 2023). The incorporation of cobalt oxide (Co_2O_3) nanoparticles can induce changes in the FTIR spectrum of polyurethane, likely due to physical or chemical interactions between the polymer matrix and the nanoparticles. Some characteristic bands indicating the presence of Co_2O_3 include: 570 cm^{-1} (Co^{2+}-O): This band is attributed to the Co-O stretching vibration, confirming the successful incorporation of cobalt oxide nanoparticles into the polymeric matrix (Wang, 2023). Its presence suggests the formation of interactions between cobalt oxide and the functional groups of PU (Bauer, 2019). Overall, the FTIR spectrum confirms the presence of cobalt oxide nanoparticles in the polyurethane matrix, as evidenced by the band at 570 cm^{-1}, which is associated with Co^{2+}-O vibrations (Chen, 2020). Figure 9 presents a thermogravimetric analysis (TGA) of polyurethane (PU) and polyurethane reinforced with cobalt oxide (Co_2O_3) nanoparticles. The graph illustrates the variation in weight loss (%) as a function of temperature (°C), enabling an evaluation of thermal stability and the impact of reinforcement on material degradation.

The black curve represents the thermal behavior of pure polyurethane, which undergoes three distinct stages of mass loss. First stage (~71.47 °C – 154 °C, 2.83% and 14.38% mass loss); this stage corresponds to the removal of adsorbed water and low-molecular-weight compounds (Vo, 2022). Second stage (~440.15 °C, 90% mass loss); at this stage, the primary structure of polyurethane degrades, involving the cleavage of urethane bonds and the decomposition of both hard and soft segments (Mikulčić, 2019). Third stage (above 450 °C): This represents the final degradation phase, leaving behind a minimal carbonaceous residue (Chen, 2023).

The effect of Cobalt Oxide (Co_2O_3) Nanoparticle Reinforcement. The red curve corresponds to PU reinforced with 1% by weight of Co_3O_4, displaying notable differences compared to pure PU; enhanced thermal stability in the initial stages; the first degradation stage occurs at a higher temperature (155 °C vs. 154 °C for pure PU).

Lower mass loss in the first and second stages. The reinforced sample exhibits a more gradual mass loss, suggesting that Co_2O_3 acts as a thermal barrier (Behnam, 2019). Higher primary degradation temperature (456.39 °C vs. 440.15 °C): This indicates improved thermal stability, likely due to interactions between the polymer matrix and the nanoparticles. Increased final residue: A greater percentage of remaining material suggests that the inorganic nanoparticles contribute to a stable residual phase (Sinh, 2019). The incorporation of Co_2O_3 enhances the thermal stability of polyurethane by reducing its degradation rate and increasing the temperature at which major decomposition occurs (Mooss, 2019).

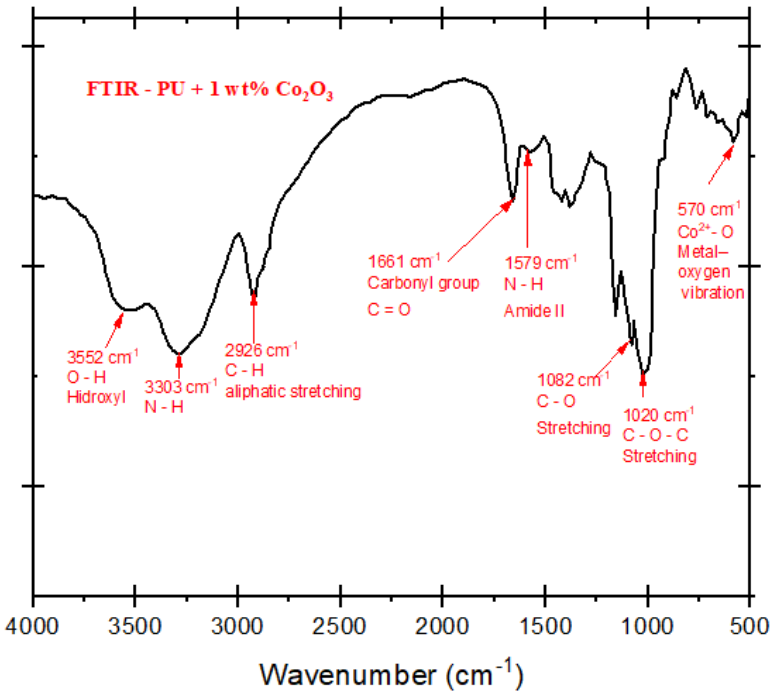


Figure 8. Fourier Transform (IR) for functional groups present in the polyurethane bonds.

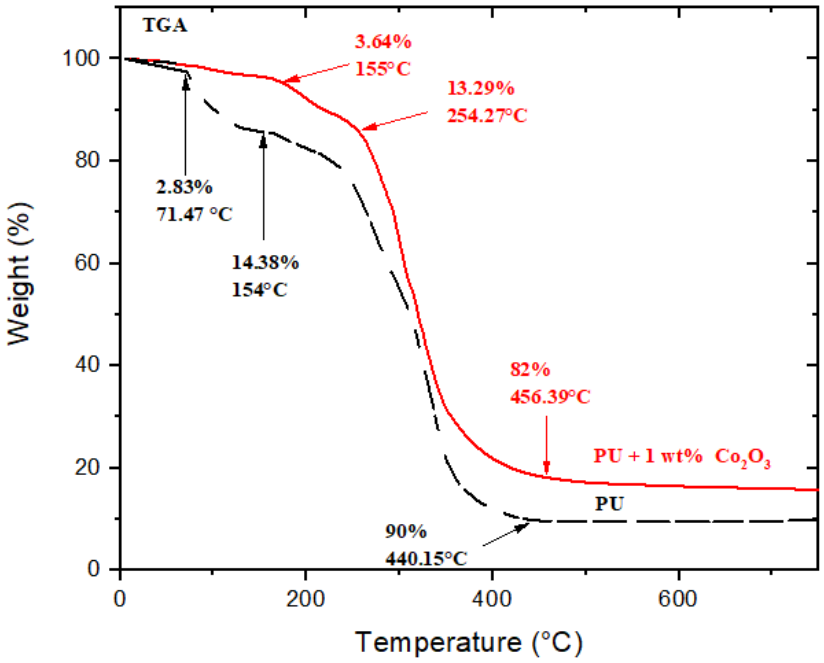


Figure 9. TGA curve of two systems.

3.3. PU tensile strength according to ASTM D638 2022

The stress-strain curve analysis shows a significant improvement in the mechanical properties of polyurethane (PU) reinforced with 1% by weight of Co_2O_3 compared to pure PU. The maximum tensile strength (UTS) of pure PU reached a value of 9.58

MPa ± 0.27 with a deformation of 43.20% before fracture, while PU with Co_2O_3 presented a ultimate tensile strength (UTS) of 16.55 MPa ± 1.47 and a deformation of 62.25%, representing a 72.8% increase in mechanical strength and a higher elongation capacity before failure. The modulus of elasticity, calculated from the slope of the elastic region of the stress-strain curve, was 22.18 MPa for pure PU and 26.59 MPa for Co_2O_3-reinforced PU, indicating an increase of 19.9%. This increase in the material's rigidity suggests that the addition of Co_2O_3 nanoparticles improves resistance to deformation, making the material stiffer and more resistant to mechanical stresses (Bahramnia, 2021).

The improvement in the mechanical properties of PU with Co_2O_3 can be attributed to several factors. First, the interaction between the polymer matrix and the nanoparticles strengthens the material by restricting the movement of the polymer chains, resulting in increased peak stress before fracture (Yazman, 2021). In addition, the incorporation of nanoparticles improves charge transfer within the material, distributing stress more evenly and reducing the spread of microcracks (Zhang, 2024). The presence of Co_2O_3 is also likely to increase interfacial adhesion between the polymer matrix and nanoparticles, contributing to higher mechanical strength (Deyab, 2024).

Another relevant aspect is the hardening effect induced by nanoparticles, as they can act as physical barriers that restrict molecular mobility within polyurethane, making it difficult to deform and increasing the overall strength of the material (Rodríguez, 2024). Taken together, these effects explain why Co_2O_3 nanoparticle-reinforced PU exhibits an optimal combination of strength and ductility, making it a promising material for applications where high mechanical strength is required along with improved deformation capacity (Raj, 2021). See Figure 10 & 11.

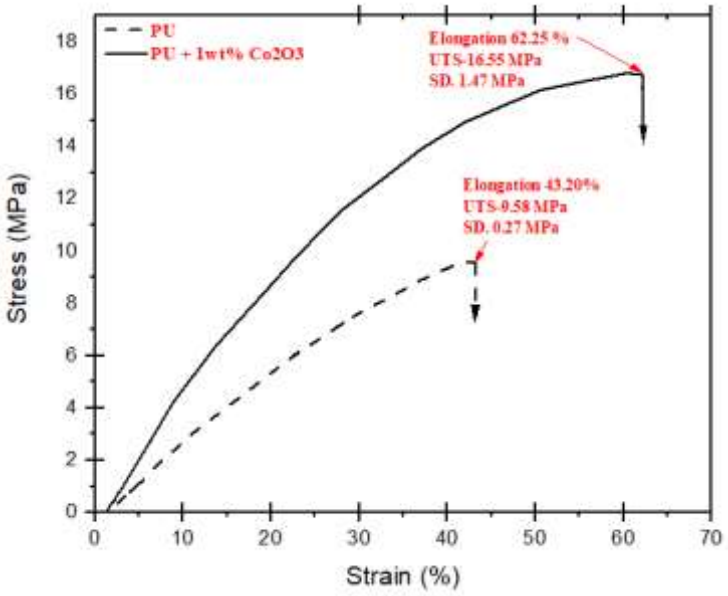


Figure 10. Stress - strain curve of two systems.

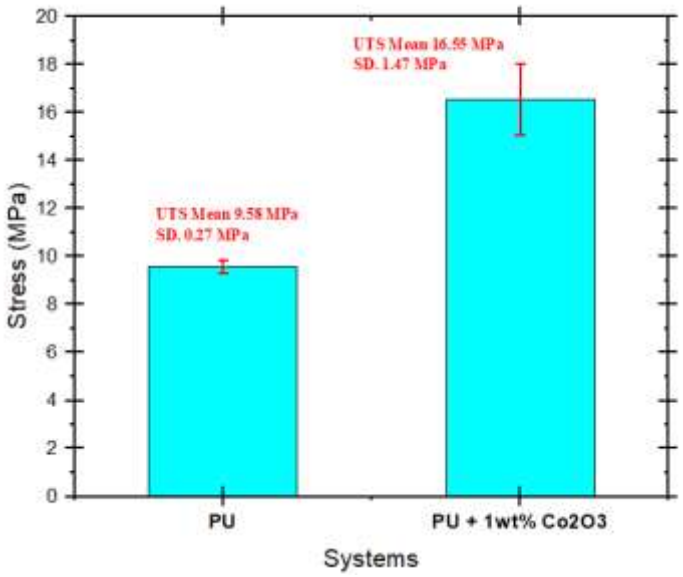


Figure 11. Bar plot of tensile strength.

3.4. Electrochemical analysis

3.4.1. The open circuit potential (OCP)

The polyurethane (PU) coating system initially exhibited a potential of -494 mV, which gradually decreased to -512 mV by the end of the experiment. This downward shift indicates a slight instability upon exposure to the saline solution, likely caused by water absorption or the formation of corrosion byproducts at the interface between the coating and the substrate (Yu, 2021). This behavior aligns with previous studies, which suggest that polymeric coatings often experience an initial drop in OCP potential when first exposed to aggressive environments (Wen, 2019). In contrast, the PU coating reinforced with 1 wt% Co_2O_3 nanoparticles started with a potential of -523 mV and remained nearly unchanged, finishing at -524 mV. The minimal variation observed in this system suggests that incorporating Co_2O_3 nanoparticles enhances the coating's corrosion resistance, likely by forming a more robust protective barrier against the infiltration of corrosive species. Previous research supports the idea that metallic nanoparticles improve the electrochemical stability of polymeric coatings by lowering permeability and enhancing corrosion protection (Dhawan et al., 2020).

Meanwhile, the uncoated 1018 steel substrate exhibited an initial potential of -560 mV, which slightly decreased to -565 mV. Although the change was minor, the more negative potential indicates a higher susceptibility to corrosion due to the absence of a protective coating. This finding is consistent with studies showing that bare metals in saline environments tend to develop increasingly negative potentials as corrosion products accumulate on the surface (Díaz, 2022). Overall, the OCP analysis revealed notable differences in the electrochemical performance of the evaluated systems. The inclusion of Co_2O_3 nanoparticles in the PU coating resulted in greater potential stability, suggesting superior corrosion protection compared to the unmodified PU coating and the uncoated steel substrate. See Figure 12.

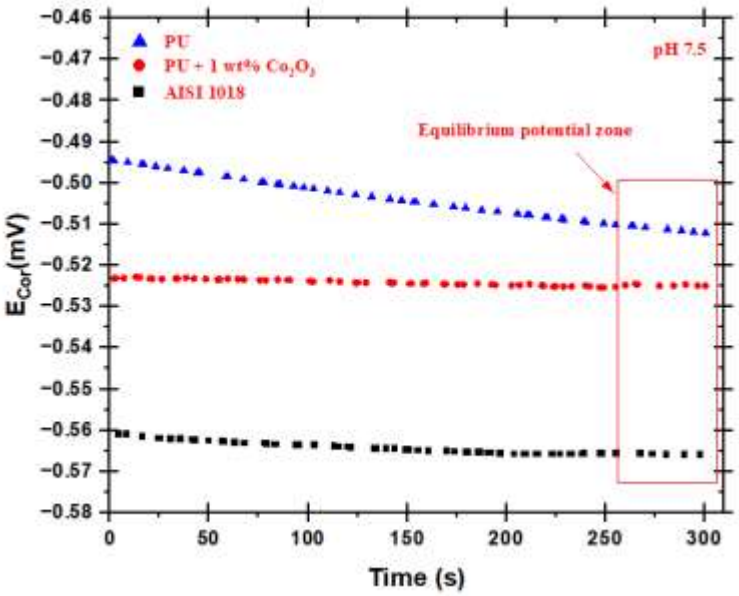


Figure 12. Open Circuit Potential measurement pH 7.5.

3.4.2. Linear polarization resistance and potentiodynamic curves

The polarization resistance of the 1wt% Co_2O_3 coating system increased to 1071 ($k\Omega/cm^2$), with respect to the bare metal material, remaining below the PU system (without reinforcement) with a value of 1390 ($k\Omega/ cm^2$), see Figure 13 (a). The resistance to polarization according to the equation of Stern and Geary, mentions that it is inversely proportional to the corrosion rate (Ropital, 2011), in the case of the reinforced system of 1% of Co_2O_3 presented a decrease, the reason is the agglomeration of the nanoparticles generated porosity in the film of the hybrid coating decreasing the magnitude of the resistance to linear polarization (Díez, 2019). See Table 4.

The results of the electrochemical analysis in a NaCl solution at a concentration of 5% showed that the uncoated system, 1018, had a corrosion potential value of -727 mV, and on the x-axis, a corrosion current density value of 37 $\mu A/cm^2$. When performing the analysis of the polyurethane (PU) coating on the AISI 1018 carbon steel substrate with the reinforced polymeric coating, 1 wt% Co_2O_3 NPs, it showed an electrochemical corrosion potential value of -587 mV, with a current density value of 4 $\mu A/cm^2$; thus, revealing a more noble behavior; in other words, less tendency to corrosion. Finally, for the steel substrate system coated only with unreinforced polyurethane (PU), a corrosion potential value of -536 mV and a current density of 3 $\mu A/cm^2$ were obtained by means of the Tafel extrapolation technique, which determined the intersection of the slopes of the cathodic and anodic lines of each of the polarization curves. Figure 13 (b) illustrates the systems for AISI 1018 and PU without cobalt oxide NP (without reinforcement). Its current density value was lower according to c (2010), anticorrosive coating systems showed noble behavior if they are close to 0.0 mV; that is, it showed considerable corrosion resistance in accordance with ASTM G3-14 (2024). Systems of a polymeric nature, particularly polyurethane-based coatings, are known to have greater nobility when analyzed using the polarization curve technique. They act as a physically-based impermeable system or barrier that prevents the transfer of energy from the circuit that generates the exchange of electrons (Salzano,

2022). The corrosion resistance in the reinforced polymer coating showed a decrease compared to the unreinforced system. The reason that Co_2O_3 NPs agglomerate along the surface of the entire coating, due to the high surface energy of NPs, they are easy to aggregate and form some agglomerates with different structures (Zhang et al., 2021), generating open spaces, allowing contact of the alkaline medium and the metal surface, generating the beginning of the electrochemical corrosion process. increasing corrosion with respect to the system without NP reinforcement (Perilla, 2019).

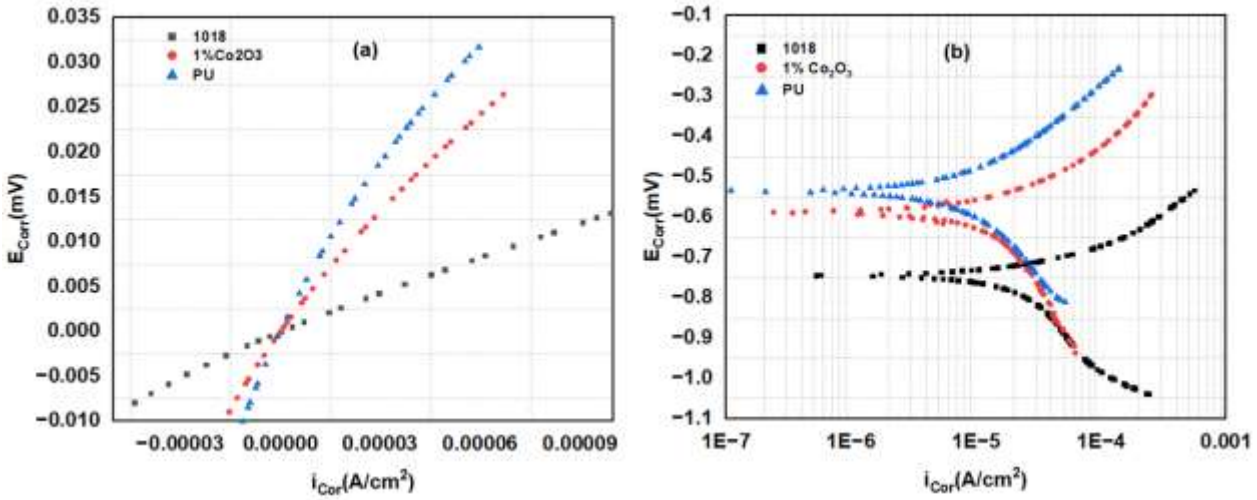


Figure 13. Polarization curves for three systems.

Table 4. Electrochemical measurements.

System	(kΩ/cm^2)	SD	βa	βc	Ecorr(mV)	SD	I cor (A/cm^2)	SD
1018	187	12	0.09	0.3	-727	4.5	37	8
1% Co_2O_3	1071	32	0.52	0.61	-587.	1	4	1
PU	1390	5	0.71	0.84	-536	2	3	1.3

3.4.3. Corrosion rate

Using Tafel's extrapolation technique, the electrochemical values for I_{corr} and E_{corr} were determined, while the corrosion rate was calculated using the Gamry software, expressed in thousandths of an inch per year (mpy), in accordance with ASTM G102-89 (2023). The uncoated system (AISI 1018), when exposed to a 5% NaCl solution, presented a corrosion rate of 25.97 ± 0.66 mpy, which confirms the susceptibility of structural steel to deterioration in saline media (Adigun, 2024). The mean graph shows a dispersion in the corrosion values of bare steel, suggesting an active progression of the corrosive process with variations in the intensity of surface degradation. On the other hand, the unreinforced polyurethane (PU) coating presented a notable reduction in corrosion speed, reaching a value of 0.008 ± 0.00137 mpy, which represents a decrease of 99.97% with respect to the base material. This result indicates that the polymer matrix acted as an effective barrier against the diffusion of corrosive species, protecting the surface of the metal substrate (Alrashed, 2019). As for the hybrid coating with 1% by weight of Co_2O_3, the corrosion rate was 0.047 ± 0.0062 mpy, reflecting a decrease of 99.81% compared to uncoated steel. However, the hybrid system showed a slight increase in corrosion rate compared to pure PU. This

0.16% increase can be attributed to the possible agglomeration of nanoparticles within the polymeric matrix, which generated localized porosity in the coating, allowing the penetration of chloride ions (Cl^-) and favoring the initiation of corrosive processes in specific areas (Radhamani, 2020). The average graph confirms this trend, showing that both PU and PU + 1 wt% Co_2O_3 have values close to zero, indicating effective protection against corrosion. However, the presence of cobalt oxide nanoparticles did not significantly improve the corrosion resistance of the pure polymer coating, indicating the need to optimize the dispersion of nanoparticles in the matrix to avoid the generation of structural defects in the protective film (Samardžija, 2022). See Figure 14.

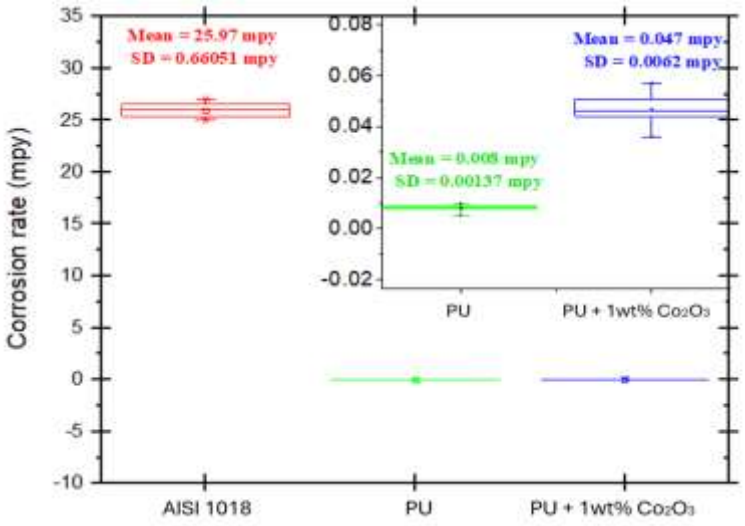


Figure 14. A comparison of corrosion rates for three different systems studied.

The coatings developed in the present work showed a significantly higher anticorrosive performance compared to various systems reported in the recent literature. In particular, the pure polyurethane (PU) coating reached a corrosion rate of 0.008 mpy, while the modified system with cobalt (III) oxide nanoparticles, PU + 1 wt% Co_2O_3 presented a speed of 0.047 mpy. These values were obtained under controlled conditions of exposure to a 5% saline solution, simulating an aggressive environment similar to that used in comparative studies. In contrast, Zhan (2025) reports that an epoxy coating reinforced with graphene oxide, also exposed to a 5% saline solution, showed a corrosion rate of 0.035 mpy, a value that, although relatively low, is higher than the pure PU coating developed in this study. This suggests that the base PU system has an effective barrier capacity against the ingress of aggressive agents, even without the presence of nanometric reinforcements. On the other hand, Mendoza (2021) reported that a coating based on polymethylmethacrylate reinforced with silicon oxides (PMMA–SiO_2) showed a corrosion rate of 9.84 mpy, a significantly higher value compared to the coatings developed in this project. This behavior could be attributed to a lower structural integrity of the PMMA–SiO_2 system against ionic attack or to a limited interaction between the matrix and the reinforcement nanoparticles, which allows a higher permeability of the solution to the metal substrate. Overall, the results obtained show that the coatings developed, particularly PU without reinforcement, present a highly efficient performance in

terms of corrosion protection, even surpassing systems reported with advanced reinforcements. The inclusion of Co_2O_3, although it increased the corrosion rate compared to the pure matrix, could be optimized through adjustments in the concentration or better dispersion of the nanoparticles, which opens an avenue for improvement in future research.

To validate the applicability of parametric statistical tests in the analysis of corrosion rate data, a normality test was conducted using the Shapiro-Wilk method, utilizing the OriginPro software and a significance level of 0.05 (5%). See Figure 15 and Table 5. This test allows determining whether the data of each analyzed group is normally distributed, which is a fundamental assumption for the use of techniques such as one-way ANOVA.

The three systems evaluated were: AISI 1018 without coating, polyurethane (PU), and PU reinforced with 1 wt% of Co_2O_3. The results obtained are summarized in the corresponding table, where in all cases the p-value was greater than 0.05, indicating that the null hypothesis of normality cannot be rejected. In particular, the AISI 1018 system presented a Shapiro-Wilk statistic of 0.96917 and a p-value of 0.88303, indicating a strong agreement with a normal distribution. Similarly, the PU system showed a p-value of 0.17615, while PU + 1 wt% Co_2O_3 presented a p-value of 0.92479; also, well above the significance threshold, confirming that their data can also be considered normally distributed.

These results allow us to conclude that the three datasets meet the assumption of normality; therefore, it is statistically valid to apply parametric analyses such as ANOVA to compare the corrosion rates among the evaluated systems. Moreover, the adherence to the normality criterion suggests that the observed differences in the mean corrosion rates are not influenced by biases in the data distribution, thus reinforcing the statistical validity of the subsequent comparative analysis.

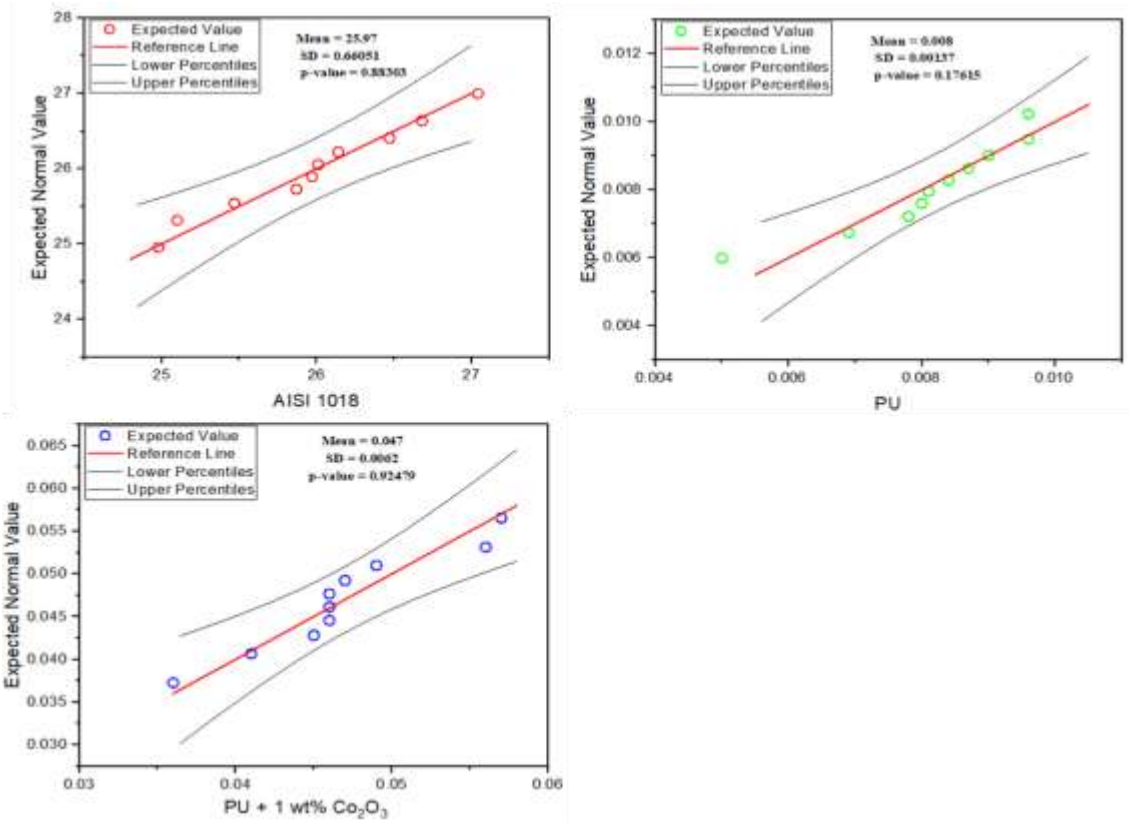


Figure 15. QQ-plot Normality Test.

Table 5. Test normality 5% Shapiro-Wilk.

Systems	DF	Statistic	p-value	Decision at level 5%
AISI 1018	10	0.96917	0.88303	normal
PU	10	0.17615	0.17615	normal
PU + 1 wt% Co_2O_3	10	0.92479	0.92479	normal

According to the one-way ANOVA, the comparison of Tukey and Fisher means with a significance level of 0.05 (95% confidence interval) shows that the corrosion rate between the systems evaluated presents statistically significant differences. Table 6 shows an F-value of 15428.76, indicating considerable variability between groups compared to within-group variability. Given the Prob > F value < 0.0001, the null hypothesis (H_0) is rejected, and the alternative hypothesis (H_A) is accepted, suggesting that at least one of the mean corrosion rates is significantly different. The Tukey and Fisher mean comparison graph (Figure 16) supports these results, showing significant differences in corrosion rate between the systems evaluated. PU and PU + 1wt% Co_2O_3 coatings have significantly lower values than uncoated 1018 steel, demonstrating their effectiveness in protecting against corrosion. In addition, Tukey's test indicates that the difference between PU and PU with 1 wt% Co_2O_3 is not significant, suggesting that the incorporation of cobalt oxide nanoparticles does not significantly improve corrosion resistance compared to pure PU.

On the other hand, Fisher's test confirms that the PU coating and its nanoparticle-reinforced version present a statistically significant difference from 1018 steel, which reinforces the effectiveness of the coatings in reducing the corrosion rate. However, the

similarity between pure PU and Co_2O_3 coating suggests that the dispersion of the nanoparticles within the polymer matrix may have influenced the generation of defects or porosity, allowing a slight increase in the coating's permeability to corrosive ions (Samardžija, 2022).

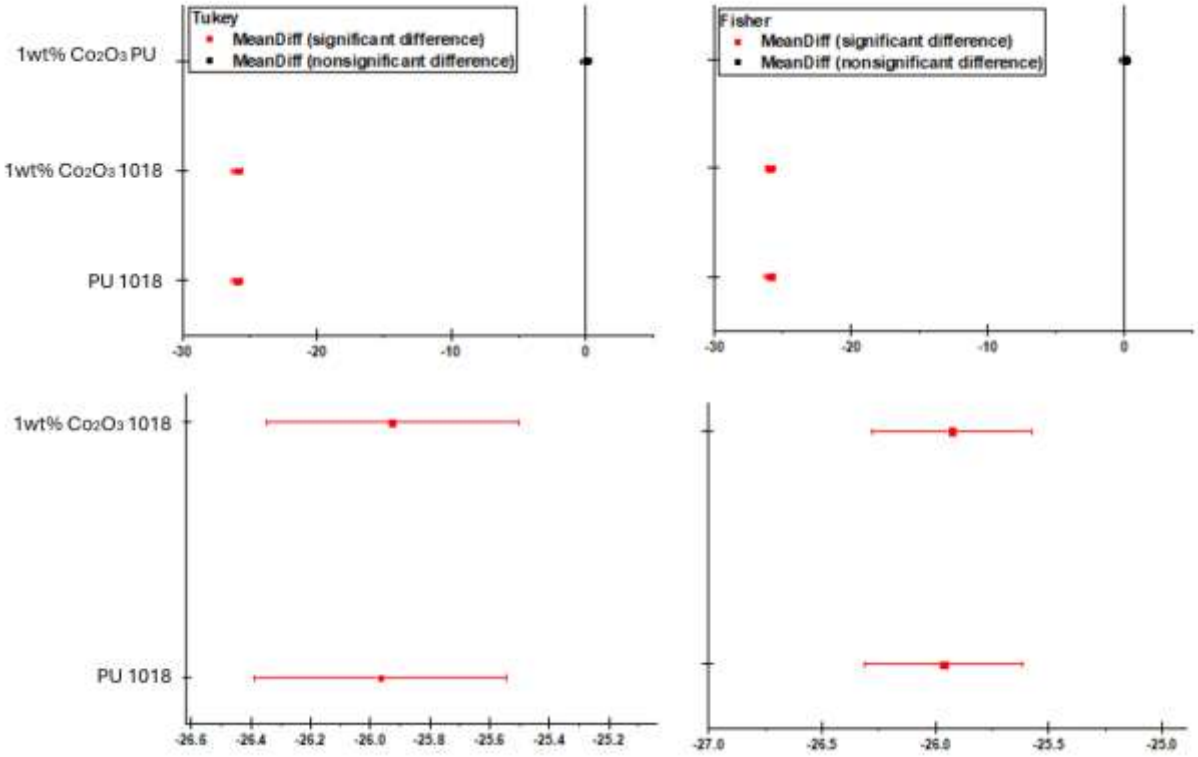


Figure 16. ANOVA one way, Tukey and Fisher Mean difference (95%).

Table 6. Overall ANOVA one way (95%).

	DF	Sum of Squares	Mean Square	F Value	Prob > F
Model	2	4487.79	2243.89	15428.76	<0.0001
Error	27	3.92	0.14		
Total	29	4491.72			

4. Conclusions

XRD analysis confirmed the formation of Co_2O_3 nanoparticles with a cubic spinel structure and high crystalline purity, with an average crystallite size of 16.83 nm. DLS analysis indicated a predominant particle size distribution between 50–100 nm, with evidence of aggregates that explain the discrepancy with the XRD results. This heterogeneity suggests that synthesis parameters strongly influenced nucleation and growth.

FTIR analysis verified the presence of the main functional groups of the PU matrix and the effective incorporation of Co_2O_3, indicating physicochemical interactions between the nanoparticles and the polymer chains. TGA demonstrated that the reinforced system exhibited enhanced thermal stability, with a shift of the main degradation stage to higher temperatures and an increase in residual mass, confirming the role of nanoparticles as thermal barriers.

Mechanical testing revealed a substantial improvement in the PU reinforced with 1 wt% Co_2O_3, with a 72.8% increase in tensile strength and higher elongation at break, evidencing simultaneous gains in strength and ductility. These results indicate that Co_2O_3 nanoparticles act as an effective dispersed phase, improving stress distribution and interfacial adhesion within the polymer matrix.

Electrochemical studies showed that pure PU achieved the best anticorrosive performance (0.008 mpy), outperforming the hybrid system (0.047 mpy), where nanoparticle agglomeration led to localized porosity and reduced barrier uniformity. Nevertheless, both coatings drastically decreased the corrosion rate of AISI 1018 steel compared to the uncoated substrate (25.97 mpy). Statistical analysis (ANOVA) confirmed significant differences between coated and uncoated systems, but no significant difference between PU and PU + Co_2O_3.

Overall, these findings demonstrate that pure PU provides excellent anticorrosive protection, surpassing several advanced systems reported in the literature. The addition of Co_2O_3 contributes significant thermal and mechanical improvements, although its anticorrosive effect depends on optimizing nanoparticle dispersion. These results support the potential application of hybrid coatings in aggressive environments while highlighting the need for improved dispersion strategies to maximize the multifunctional benefits of cobalt oxide nanoparticles.

5. References

1. Adigun, D., Bodude, A., Adigun, A. R., Adebayo, B. O. A., Umunakwue, R., Kolawole, F. O., & Borisade, G. S. (2024). Corrosion Behaviours of Austempered AISI 1018 Steel. Nigerian Journal of Engineering, 31(2), 1-1. https://www.njeabu.com.ng/fulltext/192-1685998791.pdf?1758508594.

2. Alrashed, M., Jana, S., & Soucek, M. (2019). Corrosion performance of polyurethane hybrid coatings with encapsulated inhibitor. Progress in Organic Coatings, 130, 235-243. https://doi.org/10.1016/j.porgcoat.2019.02.005.

3. Antonio, G. (2020). *Efecto de la temperatura en el proceso de soldadura sobre el endurecimiento superficial y deformación de una placa de acero A36* [Universidad Autónoma de Coahuila]. http://www.investigacionyposgrado.uadec.mx/publicacion/efecto-de-la-temperatura-en-el-proceso-de-soldadura-sobre-el-endurecimiento-superficial-y-deformacion-de-una-placa-de-acero-a36/.

4. ASTM G3-89. (2019). Standard Practice for Conventions Applicable to Electrochemical Measurements in Corrosion Testing. *ASTM Standards*, *i*(Reapproved 2019), 1–9. https://doi.org/10.1520/G0003-89R10.2

5. Bahramnia, H., Semnani, H. M., Habibolahzadeh, A., & Abdoos, H. (2021). Epoxy/polyurethane hybrid nanocomposite coatings reinforced with MWCNTs and SiO2 nanoparticles: Processing, mechanical properties and wear behavior. Surface and Coatings Technology, 415, 127121. 10.1016/j.surfcoat.2021.127121.

6. Balangao, J. K. (2024). Corrosion of metals: factors, types and prevention

strategies. Journal of Chemical Health Risks, 14(1), 79-87. https://jchr.org/index.php/JCHR/article/view/2120.

7. Bali, K., Beggas, A., & Gahtar, A. (2024). The effect of substrate temperature on the structural, morphological, optical and electrical properties of Co_3O_4 thin films. Studies in Engineering and Exact Sciences, 5(3), e12882-e12882. 10.2478/awutp-2024-0010.

8. Basak, M., Rahman, M. L., Ahmed, M. F., Biswas, B., & Sharmin, N. (2022). The use of X-ray diffraction peak profile analysis to determine the structural parameters of cobalt ferrite nanoparticles using Debye-Scherrer, Williamson-Hall, Halder-Wagner and Size-strain plot: Different precipitating agent approach. Journal of Alloys and Compounds, 895, 162694. 10.1016/j.jallcom.2021.162694.

9. Bauer, T., Agel, F., Blaumeiser, D., Maisel, S., Görling, A., Wasserscheid, P., & Libuda, J. (2019). Low-Temperature Synthesis of Oxides in Ionic Liquids: Ozone-Mediated Formation of Co_3O_4 Nanoparticles Monitored by In Situ Infrared Spectroscopy. Advanced Materials Interfaces, 6(20), 1900890. https://doi.org/10.1002/admi.201900890.

10. Behnam, R., Roghani, H., & Salami, M. (2019). Incorporation of silica nanoparticles and polyurethane into hybrid composites for increase of char residue. Journal of Thermal Analysis and Calorimetry, 135, 3311-3319. 10.1007/s10973-018-7581-4.

11. Bokuniaeva, A., & Vorokh, A. (2019, December). Estimation of particle size using the Debye equation and the Scherrer formula for polyphasic TiO2 powder. In journal of physics: Conference series (Vol. 1410, No. 1, p. 012057). IOP Publishing. 10.1088/1742-6596/1410/1/012057.

12. Chen, R., Tan, Y., Zhang, Z., Lei, Z., Wu, W., Cheng, N., & Mu, S. (2020). Hydrazine hydrate induced two-dimensional porous Co3+ enriched Co_3O_4 nanosheets for enhanced water oxidation catalysis. ACS Sustainable Chemistry & Engineering, 8(26), 9813-9821. 10.1021/acssuschemeng.0c02421.

13. Chen, X., Cai, D., Yang, Y., Sun, Y., Wang, B., Yao, Z., ... & Magdziarz, A. (2023). Pyrolysis kinetics of bio-based polyurethane: Evaluating the kinetic parameters, thermodynamic parameters, and complementary product gas analysis using TG/FTIR and TG/GC-MS. Renewable Energy, 205, 490-498. 10.1016/j.renene.2023.01.078.

14. Chérif, I., Dkhil, Y., Smaoui, S., Elhadef, K., Ferhi, M., & Ammar, S. (2023). X-ray diffraction analysis by modified scherrer, williamson–hall and size–strain plot methods of ZnO nanocrystals synthesized by oxalate route: a potential antimicrobial candidate against foodborne pathogens. Journal of Cluster Science, 34(1), 623-638. 10.1007/s10876-022-02248-z.

15. Daranfed, W., Guermat, N., & Mirouh, K. (2020, April). Experimental study of precursor concentration the Co_3O_4 thin films used as solar absorbers. In Annales de

Chimie-Science des Matériaux (Vol. 44, No. 2, pp. 121-126). 10.18280/acsm.440207.

16. Das, A, & Mahanwar, P. (2020). A brief discussion on advances in polyurethane applications. Advanced Industrial and Engineering Polymer Research, 3(3), 93-101. https://doi.org/10.1016/j.aiepr.2020.07.002.

17. Disarno, L., Majidian, A., & Karagiannakis, G. (2021). The effect of atmospheric corrosion on steel structures: A state-of-the-art and case-study. Buildings, 11(12), 571. https://doi.org/10.3390/buildings11120571.

18. Díaz, C., Cisneros, M., & Chavarín, J. U. (2022). Inhibición de la corrosión del acero 1018 en medio salino por Curcuma longa: 1018 steel corrosion inhibition in chloride media by Curcuma longa. *South Florida Journal of Development*, *3*(2), 2376-2390. 10.46932/sfjdv3n2-063.

19. de Paula, S., Aroeira, B., Souza, L. H. de O., da Cruz, A. C., Fedel, M., da Silva, B. P., & Cotting, F. (2024). Influence of Organic Coating Thickness on Electrochemical Impedance Spectroscopy Response. *Coatings*, *14*(3). https://doi.org/10.3390/coatings14030285.

20. Deyab, A., El-Shamy, O., Alghamdi, M. M., & El-Zahhar, A. A. (2024). Impact of Co_3O_4 nanoparticles on epoxy's mechanical and corrosion-resistance properties for carbon steel in seawater. Scientific Reports, 14(1), 3535. 10.1038/s41598-024-53967-4

21. Dhawan, K., Bhandari, H., Ruhi, G., Bisht, B. M. S., & Sambyal, P. (2020). Corrosion Preventive Materials and Corrosion Testing. In *Corrosion Preventive Materials and Corrosion Testing* (Issue March). CRC Press. https://doi.org/10.1201/9781315101217.

22. Díez, M. (2019). Nanoparticle reinforced polymers. *Polymers*, *11*(4). https://doi.org/10.3390/polym11040625.

23. Elfadel, G., Refat, H., El-Wahab, H. A., Salem, S. S., Owda, M. E., & Abdel Reheim, M. A. M. (2023). Preparation of new surface coating based on modified oil-based polymers blended with ZnO and CuZnO NPs for steel protection. *Scientific Reports*, *13*(1), 1–19. https://doi.org/10.1038/s41598-023-34085-z.

24. Fatimah, S., Ragadhita, R., Al Husaeni, D., & Nandiyanto, A. B. D. (2022). How to calculate crystallite size from x-ray diffraction (XRD) using Scherrer method. ASEAN Journal of Science and Engineering, 2(1), 65-76. https://ejournal.upi.edu/index.php/AJSE/article/view/37647.

25. Ferreira, C. (2023). Síntese e caracterização de óxidos do tipo espinélio como suporte para imobilização de lipases (Master's thesis, Universidade Tecnológica Federal do Paraná). https://repositorio.utfpr.edu.br/jspui/handle/1/32796.

26. Freitas, A. (2019). Synthèse de nanoparticules cristallines en solution: rôle des états transitoires

(Doctoral dissertation, Université Paris Saclay (COmUE)). https://pastel.hal.science/tel-02091181/file/74504_DE_JESUS_ALMEIDA_FREITAS_2019_archivage.pdf

27. G102-89, A. (2015). *Standard Practice for Calculation of Corrosion Rates and Related Information from Electrochemical Measurements*. *i*(Reapproved), 1–6. https://doi.org/10.1520/G0102-89R15E01.

28. Głowińska, E., Smorawska, J., Niesiobędzka, J., & Datta, J. (2024). Structure versus hydrolytic and thermal stability of bio-based thermoplastic polyurethane elastomers composed of hard and soft building blocks with high content of green carbon. Journal of Thermal Analysis and Calorimetry, 149(5), 2147-2160. 10.1007/s10973-023-12817-7.

29. Gómez, J., Menchaca, J., Pineda, J., Avilés, L., García, A., & Robles, J. (2020). Improvement of the anticorrosive and thermal properties of an Epoxy-SiO2 coating due to the presence of silicon nitride. *Progress in Organic Coatings*, *147*(January), 105735. https://doi.org/10.1016/j.porgcoat.2020.105735.

30. Huang, Z., Li, S., Ding, H., Pingyang, P., & Xinhuang, J. (2023). Diameter and Aggregation Controlled Preparation by Solvothermal Synthesis of Ultra-small Particles $CuFe_2O_4$. arXiv preprint arXiv:2301.01658. https://arxiv.org/abs/2301.01658.

31. Izarra, I., Borreguero, A., Garrido, I., Rodríguez, J. F., & Carmona, M. (2021). Comparison of flexible polyurethane foams properties from different polymer polyether polyols. *Polymer Testing*, *100*(December 2020), 107268. https://doi.org/10.1016/j.polymertesting.2021.107268.

32. Iannuzzi, M., & Frankel, G. S. (2022). The carbon footprint of steel corrosion. NPJ Materials Degradation, 6(1), 101. 10.1038/s41529-022-00318-1.

33. Perilla, J. (2019). Efectos sobre las porpiedades caracteristicas del polipropileno (PP) debido a la incorporación de de nano-agentes antioxidantes [Universidad de los Andes]. In *Universidad los Andes* (Vol. 2020, Issue 1). https://repositorio.uniandes.edu.co/entities/publication/e8516911-a740-42a7-bef0-5a3a7c688730.

34. Kausar, A., Naeem, K., Iqbal, M., Nazli, Z, Bhatti, H. N., Ashraf, A., ... & Khan, M. I. (2021). Kinetics, equilibrium and thermodynamics of dyes adsorption onto modified chitosan: a review. Zeitschrift für Physikalische Chemie, (0), 000010151520191586. 10.1515/zpch-2019-1586.

35. Khuyen, N., Han, P., Nguyen, N. T., Le, Q. B., Harjo, M., Anbarjafari, G., ... & Tamm, T. (2021). The use of laminates of commercially available fabrics for anti-stab body-armor. Polymers, 13(7), 1077. https://doi.org/10.3390/polym13071077.

36. Kim, A., Kainuma, S., & Yang, M.

(2021). Surface characteristics and corrosion behavior of carbon steel treated by abrasive blasting. *Metals*, *11*(12). https://doi.org/10.3390/met11122065.

37. Kotni, Pandey, S., Shekhar, S., Ranjan, R., & Srivastava, P. S. (2023). Corrosion of different metals/alloys in soil environment: A review. Materials Today: Proceedings. 10.1016/j.matpr.2023.04.537.
38. Kumari, S., Raturi, S., Kulshrestha, S., Chauhan, K., Dhingra, S., András, K., ... & Singh, T. (2023). A comprehensive review on various techniques used for synthesizing nanoparticles. Journal of Materials Research and Technology, 27, 1739-1763. https://doi.org/10.1016/j.jmrt.2023.09.291.
39. Li, J., Pu, Y., Li, S., He, B., & Chen, J. (2023). Orally administrated olsalazine-loaded multilayer pectin/chitosan/alginate composite microspheres for ulcerative colitis treatment. Biomacromolecules, 24(5), 2250-2263. 10.1021/acs.biomac.3c00146.
40. Lysenkov, E., & Striutskyi, O. V. (2023). Influence of filler introduction method on structure and properties of polymer composites based on polyurethane and silver nanoparticles. Composites Theory and Practice, 23. https://kompozyty.ptmk.net/pliczki/pliki/1436_2023t03_eduard-a-lysenkov-oleksandr-v.pdf.
41. Márquez, A., & Moreno-Palmerin, J. (2022). Corrosion resistance evaluation of boron-carbon coating on ASTM A-36 steel. *Revista Mexicana de Fisica*, *68*(1), 1–6. https://doi.org/10.31349/REVMEXFIS.68.011001.
42. Mendoza, J., & Rodríguez, J. (2021). Assessment of the adhesion and corrosion resistance of PMMA–SiO_2 coatings in synthetic seawater. Journal of Materials Research and Technology, 6, 820–830. https://doi.org/10.1016/j.jmrt.2021.01.085.
43. Mikulčić, H., Jin, Q., Stančin, H., Wang, X., Li, S., Tan, H., & Duić, N. (2019). Thermogravimetric analysis investigation of polyurethane plastic thermal properties under different atmospheric conditions. Journal of sustainable development of energy, water and environment systems, 7(2), 355-367. 10.13044/j.sdewes.d6.0254.
44. Mooss, A., Hamza, F., Zinjarde, S. S., & Athawale, A. A. (2019). Polyurethane films modified with polyaniline-zinc oxide nanocomposites for biofouling mitigation. Chemical Engineering Journal, 359, 1400-1410. 10.1016/j.cej.2018.11.038.
45. Nartita, R., Ionita, D., & Demetrescu, I. (2021). Sustainable coatings on metallic alloys as a nowadays challenge. Sustainability, 13(18), 10217. https://doi.org/10.3390/su131810217.
46. Panda, S., Panda, B. P., Nayak, S. K., & Mohanty, S. (2018). A review on waterborne thermosetting polyurethane coatings based on castor oil: synthesis, characterization, and application. Polymer-Plastics Technology and Engineering, 57(6), 500-522.

10.1080/03602559.2016.1275681.

47. Rabee, I., Gaid, C. B., Mekhemer, G. A., & Zaki, M. I. (2022). Combined TPR, XRD, and FTIR studies on the reduction behavior of Co_3O_4. Materials Chemistry and Physics, 289, 126367. 10.1016/j.matchemphys.2022.126367.

48. Radhamani, A., Lau, H. C., & Ramakrishna, S. (2020). Nanocomposite coatings on steel for enhancing the corrosion resistance: A review. Journal of Composite Materials, 54(5), 681-701. https://doi.org/10.1177/0021998319857807.

49. Ren, J., Lin, H., Zheng, X., Lei, W., Liu, D., Ren, T., ... & Jia, B. (2022). Giant and light modifiable third-order optical nonlinearity in a free-standing h-BN film. Opto-Electronic Science, 1(6), 210013-1. 10.29026/oes.2022.210013.

50. Rodriguez, M. (2020). Evaluacion de la aplicacion de recubrimientos Epoxi y Poliuretano alifatico para la inhibicion de la corrosion en las virolas de tuberias forzadas de la hidroelectrica Machupicchu–2019. http://repositorio.unjfsc.edu.pe/handle/UNJFSC/3857.

51. Rodríguez, V., Mendoza, D., Villaseñor, L., & Villafuerte-Segura, R. (2024). La ciencia de materiales en la evolución tecnológica. Pädi Boletín Científico de Ciencias Básicas e Ingenierías del ICBI, 12. 10.29057/icbi.v12iEspecial5.14318.

52. Ropital, F. (2011). Environmental degradation in hydrocarbon fuel processing plant: Issues and mitigation. In *Advances in Clean Hydrocarbon Fuel Processing: Science and Technology*. Woodhead Publishing Limited. https://doi.org/10.1533/9780857093783.5.437.

53. Raj, S., Kuzmin, A. M., Subramanian, K., Sathiamoorthyi, S., & Kandasamy, K. T. (2021). Philosophy of selecting ASTM standards for mechanical characterization of polymers and polymer composites. Materiale Plastice, 58(3), 247-256. 10.37358/MP.21.3.5523.

54. Saied, E, Salem, Radwan, A., ... & Fouda, A. (2021). The catalytic activity of biosynthesized magnesium oxide nanoparticles (MgO-NPs) for inhibiting the growth of pathogenic microbes, tanning effluent treatment, and chromium ion removal. Catalysts, 11(7), 821. https://doi.org/10.3390/catal11070821.

55. Salzano, M. (2022). Recent Trends in Waterborne and Bio-Based Polyurethane Coatings for Corrosion Protection. *Advanced Materials Interfaces*, *9*(11). https://doi.org/10.1002/admi.202101775.

56. Samardžija, M., Alar, V., Špada, V., & Stojanović, I. (2022). Corrosion behaviour of an epoxy resin reinforced with aluminium nanoparticles. Coatings, 12(10), 1500. https://doi.org/10.3390/coatings12101500.

57. Sinh, L., Luong, N., & Seppälä, J. (2019). Enhanced mechanical and thermal properties of

polyurethane/functionalised graphene oxide composites by in situ polymerisation. Plastics, Rubber and Composites, 48(10), 466-476. https://doi.org/10.1080/14658011.2019.1664820.

58. Souza, F, Kahol, K., & Gupta, R. (2021). Introduction to polyurethane chemistry. In Polyurethane chemistry: Renewable polyols and isocyanates (pp. 1-24). American Chemical Society. http://dx.doi.org/10.1021/bk-2021-1380.ch001.

59. Standard Practice for Operating Salt Spray (Fog) Apparatus, Astm 1 (2019). https://doi.org/10.1520/B0117-11.2.

60. Tharasan, P., Somprasong, M., Kenyota, N., Kanjana, N., Maiaugree, W., Jareonboon, W., & Laokul, P. (2022). Preparation and electrochemical performance of nanostructured Co_3O_4 particles. Journal of Nanoparticle Research, 24(6), 126. http://dx.doi.org/10.1007/s11051-022-05509-0.

61. Troya, E., & Alejandra, E. (2024). Predicción de la estructura tridimensional de enzimas con actividad degradadora de poliuretano en el año 2023. https://doi.org/10.37811/cl_rcm.v8i3.11510.

62. Valappil, R., Vijayanandan, A., & Balakrishnan, R. (2019). Decolorization of Reactive Blue 220 aqueous solution using fungal synthesized Co_3O_4 nanoparticles. Journal of Water Supply: Research and Technology, AQUA, 68(8), 675-686. http://dx.doi.org/10.2166/aqua.2019.086.

63. Valério, A., Trindade, F., Penacchio, R. F. S., Ramos, B. C., Damasceno, S., Estradiote, M. B., Rodella, C. B., Ferlauto, A. S., Kycia, S. W., & Morelhão, S. L. (2022). Proper usage of Scherrer's and Guinier's formulas in X-ray analysis of size distribution in systems of monocrystalline CeO_2 nanoparticles. arXiv preprint arXiv:2203.00866. https://arxiv.org/abs/2203.00866.

64. Vandam, J., Abrahami, S., Yilmaz, A., Gonzalez, Y., Terryn, H., & Mol, C. (2020). Effect of surface roughness and chemistry on the adhesion and durability of a steel-epoxy adhesive interface. *International Journal of Adhesion and Adhesives*, *96*, 102450. https://doi.org/10.1016/j.ijadhadh.2019.102450.

65. Vennela, A., Mangalaraj, D., Muthukumarasamy, N., Agilan, S., & Hemalatha, K. V. (2019). Structural and optical properties of Co_3O_4 nanoparticles prepared by sol-gel technique for photocatalytic application. International Journal of Electrochemical Science, 14(4), 3535-3552. https://doi.org/10.20964/2019.04.40.

66. Vera, F., Ormaza, R., Coello, J., Yanchapanta, V., & Gusqui, S. (2018). Aplicación de un diseño experimental completamente al azar para determinar la variabilidad de tamaños en la síntesis de nanopartículas magnéticas de hierro. Ciencia Digital, 2(4.1), 140-153. https://doi.org/10.33262/cienciadigital.v2i4.1.195.

67. Nguyen, B., Tran, C., Nguyen, T., Nguyen, D., ... & Hoang, D. (2022). Effect of metal oxide nanoparticles and aluminum hydroxide on the physicochemical properties and flame-retardant behavior of rigid polyurethane foam. Construction and Building Materials, 356, 129268. http://dx.doi.org/10.1016/j.conbuildmat.2022.129268.

68. Wang, A., Wang, W., Xu, J., Zhu, A., Zhao, C., Yu, M., ... & Wang, W. (2023). Enhancing Oxygen Evolution Reaction by Simultaneously Triggering Metal and Lattice Oxygen Redox Pair in Iridium Loading on Ni-Doped Co_3O_4. Advanced Energy Materials, 13(43), 2302537. http://dx.doi.org/10.1002/aenm.202302537.

69. Wang, Z., Wu, Y., Qiao, L., & Yan, Y. (2025). Decline in pitting corrosion resistance of 316 L stainless steel induced by Cr-depleted layer during tribocorrosion. npj Materials Degradation, 9(1), 23. http://dx.doi.org/10.1038/s41529-025-00569-8.

70. Wen, J., Geng, W., Geng, H. Z., Zhao, H., Jing, L. C., Yuan, X. T., ... & Wu, L. (2019). Improvement of corrosion resistance of waterborne polyurethane coatings by covalent and noncovalent grafted graphene oxide nanosheets. *ACS omega*, *4*(23), 20265-20274. 10.1021/acsomega.9b02687.

71. Wu, Q., Dai, C., Meng, F., Jiao, Y., & Xu, Z. J. (2024). Potential and electric double-layer effect in electrocatalytic urea synthesis. Nature Communications, 15(1), 1095. 10.1038/s41467-024-45522-6.

72. Yazman, Ş., Uyaner, M., Karabörk, F., & Akdemir, A. (2021). Effects of nano reinforcing/matrix interaction on chemical, thermal and mechanical properties of epoxy nanocomposites. Journal of Composite Materials, 55(28), 4257-4272. https://doi.org/10.1177/0021998321103705 9

73. Yu, M., Fan, C., Ge, F., Lu, Q., Wang, X., & Cui, Z. (2021). Anticorrosion behavior of organic offshore coating systems in UV, salt spray and low temperature alternation simulated Arctic offshore environment. Materials Today Communications, 28, 102545. 10.1016/j.mtcomm.2021.102545

74. Zhang, Y. et al. (2025). Enhancing the corrosion resistance of steel using an epoxy/graphene oxide coating in NaCl solution. Coatings, 15(4), 444. https://www.mdpi.com/2079-6412/15/4/444 https://doi.org/10.3390/coatings15040444.

75. Zhang, H., Zuo, M., Zhang, X., Shi, X., Yang, L., Sun, S., Zhong, J., Song, Y., & Zheng, Q. (2021). Effect of agglomeration on the selective distribution of nanoparticles in binary polymer blends. *Composites Part A: Applied Science and Manufacturing*, *149*(April), 106590. https://doi.org/10.1016/j.compositesa.2021.106590.

76. Zhang, J., Fan, Z., Li, B., Ren, D., & Xu, M. (2024). Study on structure–function integrated polymer-based microwave-absorption composites. Polymers, 16(17), 2472. https://doi.org/10.3390/polym16172472